Attaining 15.1% Efficiency in CZTS Solar Cells Under Indoor Conditions Through Sodium and Lithium Co-Doping

Yuancai Gong[a,b], Alex Jimenez-Arguijo[a,b], Ivan Caño[a,b], Romain Scaffidi[c,d,e,f], Claudia Malerba[g], Matteo Valentini[g], David Payno[h], Alejandro Navarro-Güell[a,b], Oriol Segura-Blanch[a,b], Denis Flandre[f], Bart Vermang[c,d,e], Alejandro Perez-Rodriguez[h,i], Sergio Giraldo[a,b], Marcel Placidi[a,b], Zacharie Jehl Li-Kao[a,b,h], Edgardo Saucedo*[a,b]

[a]Electronic Engineering Department, Universitat Politècnica de Catalunya (UPC), Photovoltaic Lab − Micro and Nano Technologies Group (MNT), EEBE, Av Eduard Maristany 10-14, Barcelona 08019, Catalonia, Spain

[b]Barcelona Center for Multiscale Science & Engineering, Universitat Politècnica de Catalunya (UPC), Av Eduard Maristany 10-14, Barcelona 08019, Catalonia, Spain

[c]imo-imomec, Hasselt University, Martelarenlaan 42, 3500 Hasselt, Belgium.

[d]imo-imomec, imec, Thor Park 8320, 3600 Genk, Belgium

[e]imo-imomec, EnergyVille, Thor Park 8320, 3600 Genk, Belgium

[f]ICTEAM, Université Catholique de Louvain, Place du Levant 3, Louvain-la-Neuve, 1348, Belgium

[g]ENEA, Casaccia Research Center, via Anguillarese 301, 00123 Rome, Italy

[h]Solar Energy Materials and Systems Group, Catalonia Institute for Energy Research (IREC), Jardins de les Dones de Negre 1, 08930 Sant Adrià de Besòs, Barcelona, Spain

[i]IN^{2}UB, Departament d'Enginyeria Electrònica i Biomèdica, Universitat de Barcelona, Carrer de Martí i Franquès 1, 08028, Barcelona, Spain

Email: edgardo.saucedo@upc.edu

Abstract

The growing demand for sustainable energy solutions to power low-power electronics, such as Internet of Things (IoT) devices, has intensified interest in indoor photovoltaic (IPV) technologies. Kesterite-based Cu_2ZnSnS_4 (CZTS) solar cells, owing to their non-toxic, earth-abundant constituents, tunable bandgap, and high absorption coefficients, are promising candidates for IPV applications. This study systematically investigates the effects of sodium (Na) doping, lithium (Li) doping, and Na–Li co-doping on the optoelectronic properties and performance of solution-processed CZTS solar cells. The comprehensive analysis reveals that Na doping significantly enhances the crystallinity and grain morphology of CZTS films, leading to improved efficiency, while Li doping alone has minimal impact. Notably, Na–Li co-doping further improves device performance to 10.1% under AM 1.5G illumination condition, surpassing both the reference and singly doped devices. The enhanced performance is attributed to the synergistic effects of Na and Li: Na promotes grain growth and reduces recombination at grain boundaries, while Li increases carrier concentration and passivates defects and grain boundaries in the absorber layer. When tested under 20 different indoor lighting conditions representative of real-world environments, the co-doped devices demonstrate exceptional adaptability and efficiency, achieving a power conversion efficiency of up to 15.1% under 3000 K illumination at an intensity of 2.93 mW cm^{-2}—the highest reported value for CZTS solar cells under indoor condition. These devices maintain high fill factor and stable open-circuit voltages across a range of color temperatures and light intensities, underlining their suitability for IPV applications. Our findings suggest that Na–Li co-doping is a promising strategy to optimize CZTS solar cells for indoor use. Future work should focus on bandgap engineering to better align the absorber properties with indoor light spectra, potentially further increasing the efficiency of kesterite-based solar cells in IPV applications.

Introduction

The increasing demand for sustainable and eco-friendly energy solutions has accelerated advancements in photovoltaic (PV) technology, with the emerging field of indoor photovoltaics (IPV) gaining significant attention as a promising new focus in PV research.[1,2] With the proliferation of Internet of Things (IoT) devices, wireless sensors, and other low-power electronics, the need for reliable energy harvesting from ambient indoor light sources—such as LEDs and fluorescent lamps—has become increasingly critical to reduce the reliance on disposable batteries and their associated environmental impact. Indoor PV systems, which convert artificial light or low-intensity scattered solar light into electrical energy, offer a promising solution to power these devices.[3] However, developing ideal IPV absorber materials and device architectures presents unique challenges due to the significantly lower irradiance levels and narrower wavelength spectrum indoors compared to outdoor sunlight.

Among the various material candidates for indoor photovoltaics, kesterite-based $Cu_2ZnSn(S_xSe_{1-x})_4$ (CZTSSe) solar cells stand out due to their favorable properties, including non-toxic, earth-abundant constituents, tunable bandgap, and high absorption coefficients.[4] Kesterite is considered an extremely promising IPV absorber candidate compared to conventional silicon, chalcopyrite (CIGS), CdTe, and lead-based perovskite solar cells, which either suffer from low of efficiency under low-intensity light[5] or involve toxic and rare-earth elements, as well as stability issues. In particular, concerns about toxicity and long-term stability are paramount as IPV devices are integrated into IoT systems operating in living environments where humans are in close proximity.[6,7] Kesterite's non-toxic composition and excellent long-term stability make it an ideal match for the requirements of an IPV absorber. While the efficiency of kesterite solar cells under outdoor conditions (AM 1.5G) has steadily increased in recent years,[8,9] reaching over 15%,[10] their performance under indoor lighting conditions remains largely underexplored.[11–13]

Compared to PV cells designed for standard outdoor conditions, IPV devices require careful consideration of two key factors: (1) alignment between the absorber layer's bandgap and the narrow spectral distribution of artificial light sources—typically around 1.7 to 2.0 eV for optimal photon energy utilization[14,15]— and (2) high shunt resistance to minimize the impact of leakage currents on the open-circuit voltage (V_{OC}) and fill factor (FF), usually degraded under low-light conditions.[11,16] Previous studies have reported significant drops in V_{OC} and FF when the illumination changes from standard outdoor conditions (AM 1.5G) to low-intensity halogen lamp lighting for various kesterite-based materials such as CZTSe, CZTSSe, and CZTS, resulting in poor device performance[11]. This highlights the critical importance of bandgap alignment and shunt resistance management in designing efficient IPV devices. Pure sulfide kesterite (CZTS), with a typical bandgap (E_g) of approximately 1.55 eV,[17] aligns with the spectral characteristics of indoor light sources, which predominantly emit in the visible range (380–740 nm). However, shunt resistance in CZTS solar cells is often compromised due to the presence of secondary phases, abundant point defects, unpassivated grain boundaries, severe interface recombination, and unfavorable morphology.[18] To overcome these challenges, recent research has focused on doping kesterite absorbers with extrinsic elements, particularly alkali elements such as sodium (Na), lithium (Li), and potassium (K).[19,20] These elements have demonstrated the ability to passivate defects, improve grain growth, and enhance the optoelectronic properties of the kesterite absorber.

It is well documented that relatively heavy alkali doping (e.g., Na, K) is beneficial for increasing the grain size of thin films and significantly improving morphology, while light alkali doping (e.g., Li) significantly enhances the carrier concentration and passivates the grain boundaries of the absorber.[19–22] Na has been shown to significantly improve the crystallinity and grain morphology of kesterite films, promoting larger grains and reducing recombination losses at grain boundaries[19,20]. This effect is attributed to the ability of Na to form low-temperature Na_2Se_x liquid phases, which act as fluxing agents and facilitate grain growth

during annealing. Moreover, Li is known to enhance the performance of selenide (CZTSe) and sulfo-selenide (CZTSSe) solar cells by passivating defects[23,24], forming downward band bending at grain boundaries[25], and improving carrier concentration[21], thereby boosting V_{OC}, FF, and overall device efficiency. Recent studies have demonstrated that Li doping significantly improves the efficiency of CZTSSe solar cells due to the enhancement of carrier concentrations contributed by Li_{Zn} defect formation, creating beneficial shallow acceptor defects that enhance p-type conductivity[21,26]. However, investigations into light alkali doping (Li) for sulfide kesterite (CZTS) remain scarce. The potential of Li doping to improve the optoelectronic properties of the absorber and enhance the efficiency of CZTS solar cells is still underexplored. Furthermore, co-doping with heavy and light alkali is expected to synergistically improve grain morphology, increase carrier concentration, passivate grain boundaries, and mitigate detrimental defects, resulting in reduced recombination losses and significantly enhanced device performance.

In this study, we decoupled the effects of Na doping, Li doping, and Na-Li co-doping on the film growth, grain morphology, optoelectronic properties, and final device performance of CZTS thin films. Through a series of detailed characterizations,we found that Na introduction significantly improved the grain size of the films, enhanced their optoelectronic properties, and improved device performance. In contrast, Li introduction alone had very limited positive effect on film morphology and optoelectronic properties. However, when both Na and Li were introduced, the device performance was further improved relative to Na doping alone. This enhancement stems from the synergistic effects of Li and Na, which not only enhance the crystalline quality of the films and yield larger grains but also effectively increase carrier concentration, passivate grain boundaries, and mitigate defects within the films. Consequently, the photovoltaic properties were significantly improved, leading to a CZTS solar cell with an efficiency of 10.1% under AM1.5G condition.

Furthermore, we explored the application of highly efficient Na-Li co-doped CZTS solar cells for indoor PV applications, focusing on understanding their performance under different indoor lighting conditions. The devices were characterized under 20 different irradiation conditions, corresponding to five different color temperature light spectra (2700 K, 3000 K, 4000 K, 5000 K, and 6000 K) and four different irradiances (from 3 mW cm^{-2} to 0.01 mW cm^{-2}), which are typically encountered in real-world indoor environments. Our results demonstrate a Na-Li co-doped champion device with a power conversion efficiency (PCE) of 15.1% under 3000 K lighting and 2.93 mW cm^{-2} of irradiance. The high IPV efficiency of the device is attributed to its exceptionally high shunt resistance, which dominates the device's behavior under low light intensities by minimizing leakage currents and maintaining stable V_{OC} and higher FF. While the current bandgap (1.55 eV) is not fully optimized for indoor light utilization, our findings suggest that enhancing grain growth, passivating defects, and improving carrier density through alkali co-doping offers a promising pathway for optimizing CZTS materials for indoor applications. Future research should focus on fine-tuning the bandgap and further exploring the synergistic effects of alkali co-doping to maximize the efficiency of indoor photovoltaic devices.

Results and Discussion

Effects of alkali doping on Kesterite absorber quality and device performance

The solution-processed Cu_2ZnSnS_4 (CZTS) solar cells were fabricated through three keys steps: (1) Precursor preparation: Copper(I) chloride (CuCl), zinc acetate [$Zn(OAc)_2$], and tin(IV) chloride pentahydrate ($SnCl_4 \cdot 5H_2O$) were dissolved in N,N-Dimethylformamide to create the precursor solution; (2) Spin-coating and annealing: The solution was spin-coated onto substrates, then annealed to form solid precursor films; and (3) Chalcogenide atmosphere annealing: The films were annealed in a chalcogenide-

rich atmosphere to promote crystallization and grain growth.[27,28] Detailed methodologies are provided in the Experimental Section. To control Na diffusion, soda-lime glass (SLG) substrates with a SiO_x barrier layer were used. Lithium perchlorate ($LiClO_4$) and sodium perchlorate ($NaClO_4$) were selected as alkali sources due to their solubility and thermal stability, as listed in the Table S1. High concentrations (0.5M) of these alkalis were spin-coated onto the precursor films as top layers, as schematically illustrated in **Figure 1a**, thereby avoiding potential alterations of the precursor solution chemistry that could occur with alkali introduction into the solution. By introducing Na and Li, we systematically assessed their individual and combined impacts on device performance.

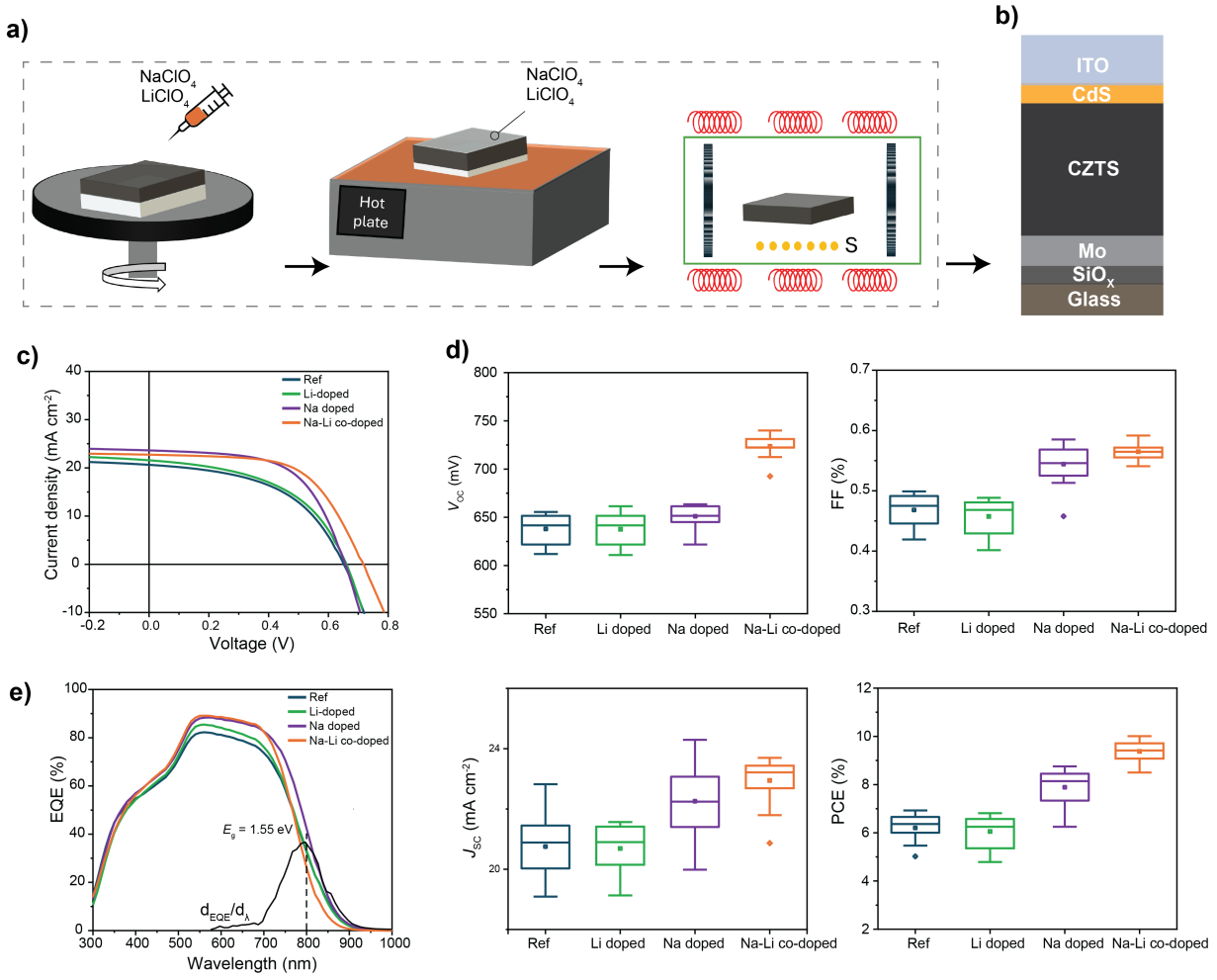

Figure 1. (a) Schematic illustration of the alkali-doped thin film preparation process. (b) Diagram of the complete CZTS solar cell structure. (c) J-V curves of the Ref and alkali-doped samples under AM1.5G illumination. (d) Box plots showing the statistical distributions of photovoltaic parameters (V_{OC}, FF, J_{SC}, and PCE) for the Ref and alkali-doped samples. (e) EQE spectra of the Ref and alkali-doped samples, with the E_g indicated for comparison.

Figure 1b depicts the configuration of the CZTS solar cell, comprising a Glass/Mo/CZTS/CdS/ITO structure. The representative current density–voltage (J–V) curves of the solar cells, shown in **Figure 1c**, reveal the substantial impact of different alkali doping strategies on device performance under standard AM 1.5G illumination. Statistical box plots of the key photovoltaic parameters V_{OC}, short-circuit current density (J_{SC}), FF, and PCE are presented in **Figure 1d**, further highlighting the distinct improvements brought about

by Na and Na-Li co-doping. The reference (Ref) device exhibits the poorest performance across all photovoltaic metrics, with a PCE of approximately 6%. Upon Li doping, the device performance shows only modest improvement, indicating that Li doping alone does not significantly enhance CZTS performance. In contrast, Na doping leads to substantial improvements across all PV metrics, particularly in FF and PCE. This suggests that Na introduction significantly enhances charge carrier transport and reduces device resistance, likely due to improved crystallinity and larger grain size, which will be discussed in a later section. The most notable performance boost is observed with Na-Li co-doping. The co-doped device achieves the highest values for V_{OC} (722 mV), J_{SC} (23.4 mA cm^{-2}), FF (59.3%), and PCE (10.1%). Specifically, the Na-Li co-doped CZTS device demonstrates an increase in V_{OC} due to the increase the carrier concentration, reduced non-radiative recombination and potential grain boundary passivation, which will be discussed in detail in the following section. The FF is improved as a result of reduced series resistance and enhanced charge carrier transport, benefiting from the synergistic effects of both Na and Li. Consequently, the PCE is elevated from 6.4% in the Ref device to 10.1% in the Na-Li co-doped device, representing a significant overall efficiency enhancement.

The external quantum efficiency (EQE) spectra (**Figure 1e**) provide further insights into the impact of alkali doping on the optical and electronic properties of the CZTS devices. The Ref device exhibits a broad EQE response peaking between 500 and 700 nm, corresponding to a E_g of approximately 1.55 eV, but with lower overall EQE values compared to the alkali-doped devices, indicating higher recombination losses and less efficient photon-electron conversion. Li doping results in a modest improvement in EQE, suggesting slight enhancement in charge collection efficiency. In contrast, Na doping significantly improves the EQE across the 500–900 nm range, indicating reduced recombination losses. The slight reduction in bandgap to 1.53 eV further supports enhanced light harvesting, particularly in the near-infrared region. The Na-Li co-doped device achieves the highest EQE across the spectrum, demonstrating that the co-doping strategy minimizes recombination and maximizes charge collection by improving absorber quality, resulting in superior overall device performance. The Urbach energy (E_U) was derived from the EQE data (Figure S1). The Ref, Li-doped, and Na-doped samples exhibit similar E_U values around 38 meV, indicating comparable levels of band tailing. However, the Na-Li co-doped sample shows a lower E_U of 34 meV, suggesting reduced band tail states associated with defects such as Cu_{Zn} and $[2Cu_{Zn} + Sn_{Zn}]$.[29,30] This reduction suggests that Li helps suppress detrimental defects, which directly contributes to the improved V_{OC} and PCE of the device. The lower E_U in the Na-Li co-doped sample highlights the effectiveness of co-doping in enhancing absorber quality and overall device performance.

To understand the mechanisms underlying the performance enhancements observed with different alkali doping strategies, we conducted detailed analyses of the films before and after sulfurization using X-ray diffraction (XRD), Raman spectroscopy, and scanning electron microscopy (SEM). The XRD patterns of the precursor films (**Figure 2a**) display diffraction peaks which correspond to the (211), (204), and (312) planes of the kesterite phase. Their broad width and weak intensity are indicative of a low-crystallinity kesterite structure. Notably, no secondary phases are observed in the precursor films, suggesting a pure kesterite composition free from impurities. Additionally, no peaks corresponding to $NaClO_4$ or $LiClO_4$ are detected, implying that these compounds, if present, are likely amorphous and reside on the film surface. Raman spectroscopy (**Figure 2d**) complements the XRD findings by confirming the presence of low-crystallinity kesterite phases in the precursor films. In the Na-Li co-doped films, vibrational peaks attributed to $(ClO_4)^{-1}$ at around 930 cm^{-1} are detected, indicating the presence of these compounds on the film surface. This suggests that the alkali salts remain on the surface in an amorphous state after spin-coating and before sulfurization. Additionally, the presence of $LiClO_4$ and $NaClO_4$ on the film surface is further confirmed by SEM image shown in **Figure S2**.

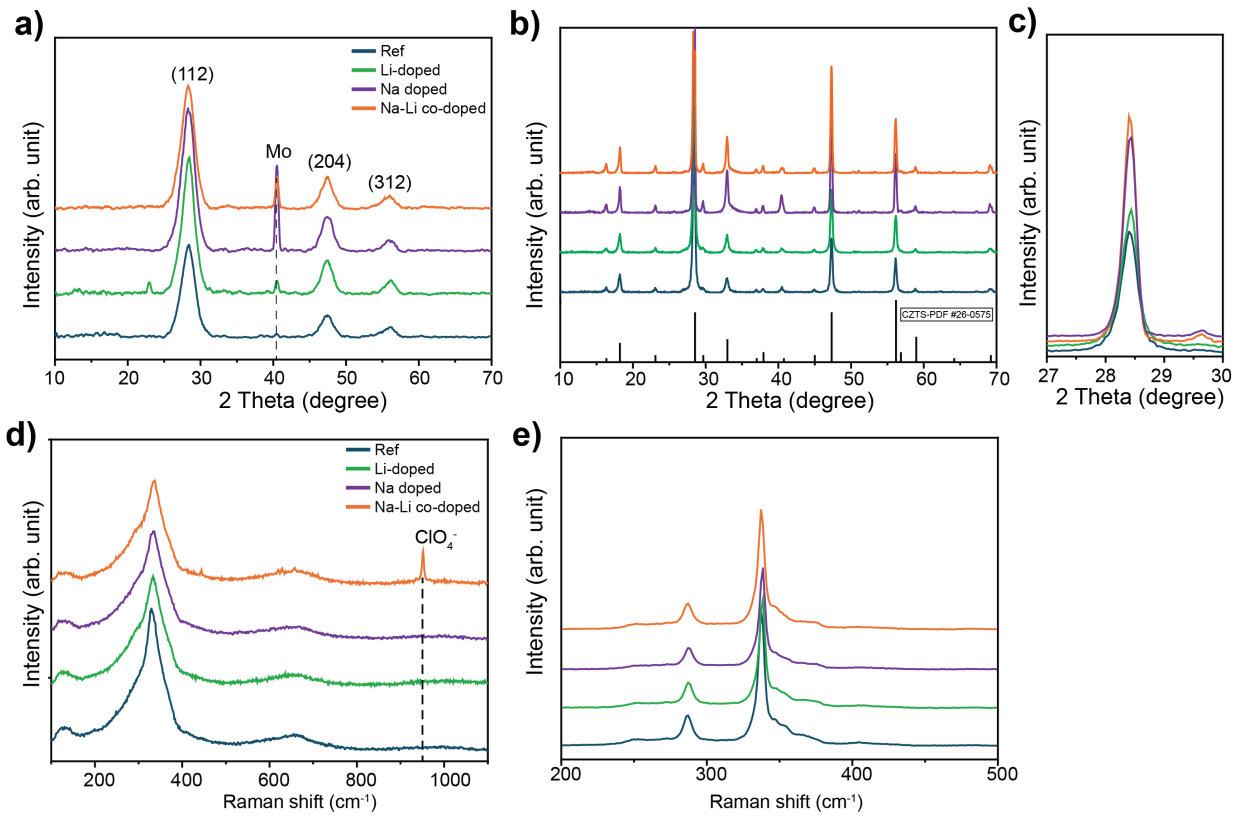

Figure 2. (a) XRD patterns of each precursor films (Ref, Li-doped, Na-doped, and Na-Li co-doped). (b) XRD patterns of the absorber films after sulfurization, showing enhanced crystallinity. (c) Enlarged view of the (211) peak from panel (b), highlighting differences in peak intensity and FWHM among the samples. (d) Raman spectra of the precursor film and (e) absorber films.

It has been previously reported that low-crystallinity kesterite films undergo a direct, single-phase transformation from an amorphous kesterite structure to a highly crystalline absorber layer during heat treatment in a chalcogenide atmosphere (S or Se).[27,28,31] This transformation pathway avoids the formation of secondary phases and is critical for preparing high-quality kesterite films. Our findings are consistent with this mechanism. After sulfurization, the XRD patterns of the absorber layer films (**Figure 2b**) reveal a significant improvement in crystallinity. The characteristic peaks of kesterite become sharper and more intense, indicating larger grain sizes and enhanced crystal ordering. Notably, the Na-doped and Na-Li co-doped films exhibit stronger diffraction peaks with narrower full width at half maximum (FWHM) values, as shown in the zoomed (211) peak (**Figure 2c**). This observation suggests that Na plays a crucial role in promoting grain growth and improving crystallinity. In contrast, the Li-doped films do not show significant enhancement in crystallinity; the diffraction peaks remain relatively broad and weak compared to the Na-doped and Na-Li co-doped films. As mentioned above, this aligns with previous studies indicating that Na facilitates the formation of a Na_2S_x liquid phase during sulfurization, which acts as a flux to promote grain growth and improve crystal quality. [32] Raman spectroscopy of the absorber films (**Figures 2e**) further corroborates the XRD results. The Raman spectra reveal distinct peaks at 285 and 330 cm^{-1}, associated with kesterite CZTS, with no detectable secondary phases such as ZnS or SnS. The absence of secondary phases in both XRD and Raman analyses emphasizes the effectiveness of Na doping in enhancing crystallinity without introducing unwanted compounds.

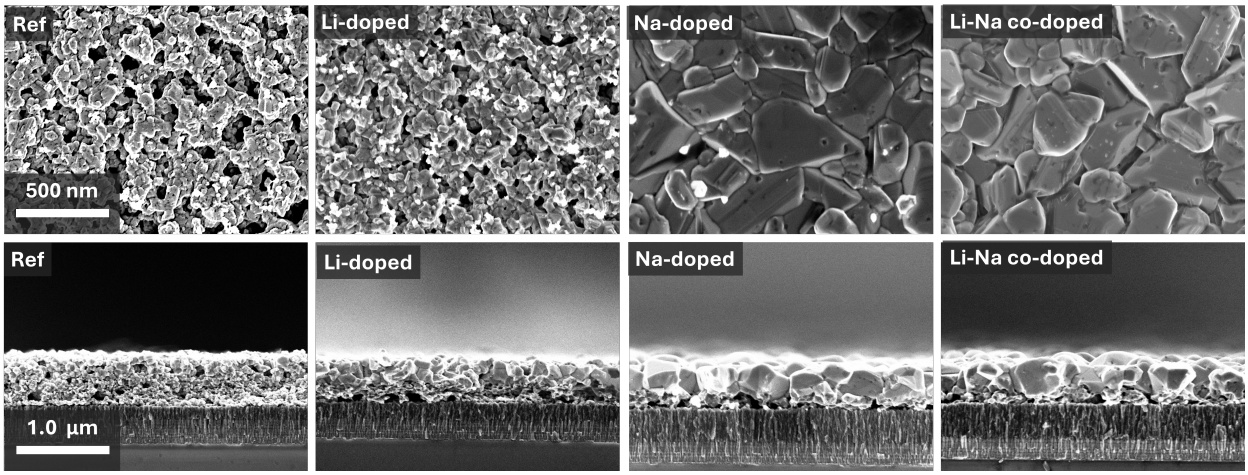

Figure 3. Top-view (top row) and cross-sectional (bottom row) SEM images of the Ref and alkali-doped (Li-doped, Na-doped, and Na-Li co-doped) absorber layers.

SEM images presented in **Figure 3** further illustrate the significant impact of alkali doping on the grain morphology of CZTS thin films. The Ref film exhibits small, irregular grains with numerous grain boundaries, likely serving as recombination centers that limit device performance. This observation aligns with the poor crystallinity indicated by the broad and weak peaks in the XRD patterns and correlates with the low efficiency metrics of the Ref devices. The Li-doped film shows only minor improvements in grain size and morphology compared to the Ref. The SEM images and XRD patterns of the Li-doped film remain similar to those of the Ref, suggesting that Li alone does not significantly improve crystallinity or promote grain growth. In contrast, the Na-doped film displays much larger, well-defined grains with reduced grain boundary density, as evidenced by the SEM images. This improved grain morphology corresponds with sharper and more intense peaks in the XRD patterns, indicating enhanced crystallinity and larger grain sizes. The larger grains and fewer grain boundaries lead to decreased recombination and improved charge transport, resulting in significant enhancements in device parameters such as J_{SC}, FF, and PCE. The Na-Li co-doped film exhibits grain morphology similar to that of the Na-doped film, with no significant further improvement in grain size or uniformity observed in the SEM images. Despite the similar crystal morphology, the Na-Li co-doped films demonstrate better optoelectronic properties compared to the Na-doped films.

To analyze the depth distribution of elements within the films and understand the effects of Na and Li incorporation, we employed glow discharge optical emission spectroscopy (GDOES). The results, shown in **Figure S3a-e**, indicate that the primary kesterite elements—Cu, Zn, Sn, and S—are uniformly distributed throughout the depth in each sample. A clear Na signal is present in the Ref sample, suggesting that despite the application of a SiO_x layer beneath the Mo as a Na diffusion barrier (**Figure 1b**), Na migration from the substrate into the CZTS layer still occurs at the high annealing temperature of 640 °C. However, this substrate-derived Na did not significantly enhance film morphology, likely due to its low concentration. So, Na diffusing from the SLG does not dominate the absorber quality enhancement. In the Na-doped samples (Na-doped and Na-Li co-doped), the Na signal is significantly stronger, indicating successful incorporation of Na from the spin-coated $NaClO_4$ layer. Interestingly, in the Li-doped samples (Li-doped and Na-Li co-doped), almost no Li is detected, while the Na content is notably higher than in the samples without Li (Figure S3e). GDOES analysis of the precursor film (Figure S3f) confirms a substantial Li presence on the film surface before sulfurization, indicating that Li is not lost during the spin-coating process.

Yang et al. previously reported on the competitive exchange behavior between Na and Li in kesterite films, where Na tends to repel Li from the film and their interaction promotes Na diffusion[33]. This phenomenon explains the consistent observation of significant Li loss during experiments. Our study aligns with this mechanism, showing that Na repels Li during the high-temperature sulfurization process, leading to severe Li depletion and its undetectability via GDOES in the final films. This Na-Li exchange mechanism results in Li effectively enhancing the Na content within the film, as illustrated in Figure S3e.

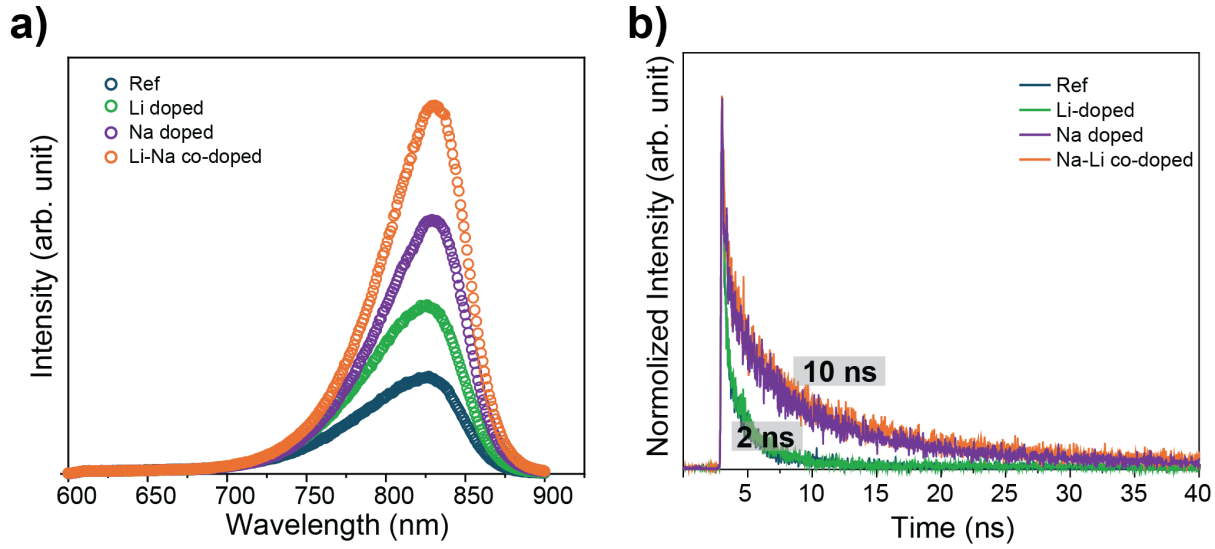

Figure 4 (a) Photoluminescence (PL) spectra and (b) time-resolved photoluminescence (TRPL) spectra of the Ref and alkali-doped (Li-doped, Na-doped, and Na-Li co-doped) absorber layers.

Photoluminescence (PL) and time-resolved photoluminescence (TRPL) measurements were conducted to elucidate the role of alkali doping in enhancing the optoelectronic properties of CZTS devices (**Figure 4**). The Ref sample exhibits the weakest PL intensity and the shortest carrier lifetime (approximately 2 ns), indicating a high density of recombination centers. This high recombination rate leads to poor charge collection and low device performance, consistent with the inferior PV metrics observed. Li doping results in a slight increase in PL intensity, reflecting modest improvements in reducing recombination losses. However, the overall effect on device performance remains limited, aligning with the minimal enhancements observed in the J–V characteristics. In contrast, Na doping significantly enhances PL intensity and extends the carrier lifetime to approximately 10 ns. The increased PL intensity and carrier lifetime indicate improved absorber quality and reduced non-radiative recombination, likely due to enhanced crystallinity and fewer grain boundaries facilitated by Na incorporation, which correlates with better device performance. The Na–Li co-doped device exhibits the highest PL intensity among all samples studied, indicating a further reduction in recombination. This enhanced PL behavior is attributed to the synergistic effect of Na and Li co-doping. The introduction of Li alongside Na likely promotes the formation of beneficial shallow defect states such as Li_{Cu}, Li_{Zn}, and V_{Cu}, which enhance p-type conductivity, and help passivate detrimental defects and grain boundaries of absorber.[21,26,34]

Alkali doping is known to increase the carrier concentration for the kesterite, thereby improving overall device performance. To quantify this effect, capacitance–voltage (C–V) measurements were performed, and the results are presented in **Figure S4**. The Ref and Na-doped devices exhibit similar carrier concentrations, around 2×10^{16} cm^{-3}. However, Na–Li co-doping significantly increases the carrier concentration to approximately 6×10^{16} cm^{-3}. This substantial increase in carrier concentration can be

attributed to two primary factors, as reported in both DFT and experimental literature: 1) Formation of shallow acceptors: the incorporation of Li into the film leads to the formation of shallow acceptor defects such as Li_{Cu} and Li_{Zn},[21,26,34] enhancing p-type conductivity, 2) Assisting Na incorporation: Li facilitates a higher Na content within the film, as observed in the GDOES analysis. The increased Na content promotes the formation of beneficial copper vacancies (V_{Cu}), further improving carrier density.[35]

Efficient CZTS Solar Cells for Indoor Photovoltaic Applications

As mentioned before, for optimal performance in indoor conditions, the IPV device needs to meet two key criteria: (1) a bandgap of 1.7–2.0 eV to match typical indoor light spectra, [15] and (2) high shunt resistance to minimize leakage currents, especially under low-light conditions where recombination losses dominate. [36] . In this study, the champion CZTS device features an absorber layer with a bandgap of 1.55 eV. Although this is somewhat lower than the ideal value for indoor photovoltaics, it demonstrates the potential for further performance improvement through bandgap tuning.

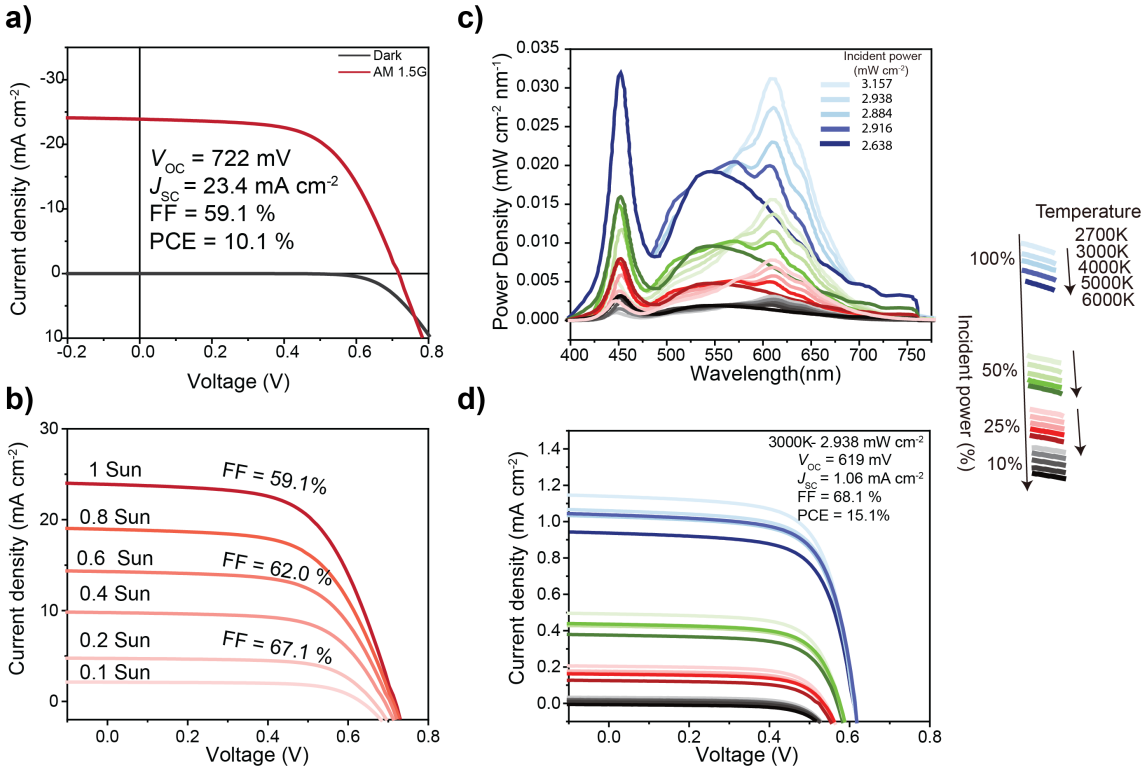

Figure 5. (a) J-V curves of the champion CZTS device under AM1.5G illumination and in dark conditions. (b) J-V curves of the CZTS device under varying light intensities. (c) Spectra of 20 typical indoor lighting conditions, representing five color temperatures (2700K, 3000K, 4000K, 5000K, and 6000K) with four intensity levels for each temperature. The maximum incident power (100%) for each color temperature spectrum is summarized in (c), and the detailed incident power for each spectrum is summarized in Table S2. (d) J-V curves of the CZTS device under the 20 different indoor light spectra presented in (c), illustrating device performance across a range of indoor lighting scenarios.

Our results demonstrate that high-efficiency CZTS solar cells exhibit remarkable adaptability and efficiency under varying lighting conditions, including both simulated sunlight (AM 1.5G) and artificial indoor

lighting. **Figure 5a** shows the J–V curve of the champion CZTS device under AM 1.5G illumination and dark conditions. The device displays a high shunt resistance (~10000 Ω·cm²), which is ideal for indoor PV applications. The device's response to varying light intensities under the AM 1.5G spectrum is shown in **Figure 5b**. As the light intensity decreases from 1 sun to 0.1 sun, the FF improves from 59.1% to 67.1%, with only a slight reduction in V_{OC}. The stability of V_{OC} across these intensities indicates that the device effectively minimizes carrier recombination losses. This demonstrates that CZTS solar cells efficient harvest energy under low-light conditions, such as scattered sunlight commonly found indoors during the day.

Figure 5c provides spectrum for 20 different indoor lighting conditions used to characterize device performance in this study, including five color temperature lights (2700 K, 3000 K, 4000 K, 5000 K, and 6000 K) and four intensity levels for each temperature light. We used this wide range of spectra for performance testing, rather than a single-color temperature and illumination intensity, to accurately evaluate the real-world performance of solar cells under complex lighting conditions and to simulate the device's operation in realistic indoor environments. **Figure 5d** presents the J–V curves under the various indoor lighting conditions depicted in Figure 5c. The device maintains high FF values under most of these conditions, and although V_{OC} shows a slight drop compared to 1 sun illumination, the overall efficiency remains high, the PV parameters are detailed in **Table 1** and **Table S2**. Under specific conditions, particularly those with high intensities and warm color temperatures (such as 2700K and 3000 K), the CZTS device achieves a power conversion efficiency (PCE) of up to over 15.0%, putting the evidence its suitability for indoor PV applications. The slight decrease in V_{OC} under low-light conditions is consistent with the expected influence of light intensity on V_{OC}; however, the higher FF values help to maintain a high PCE overall.

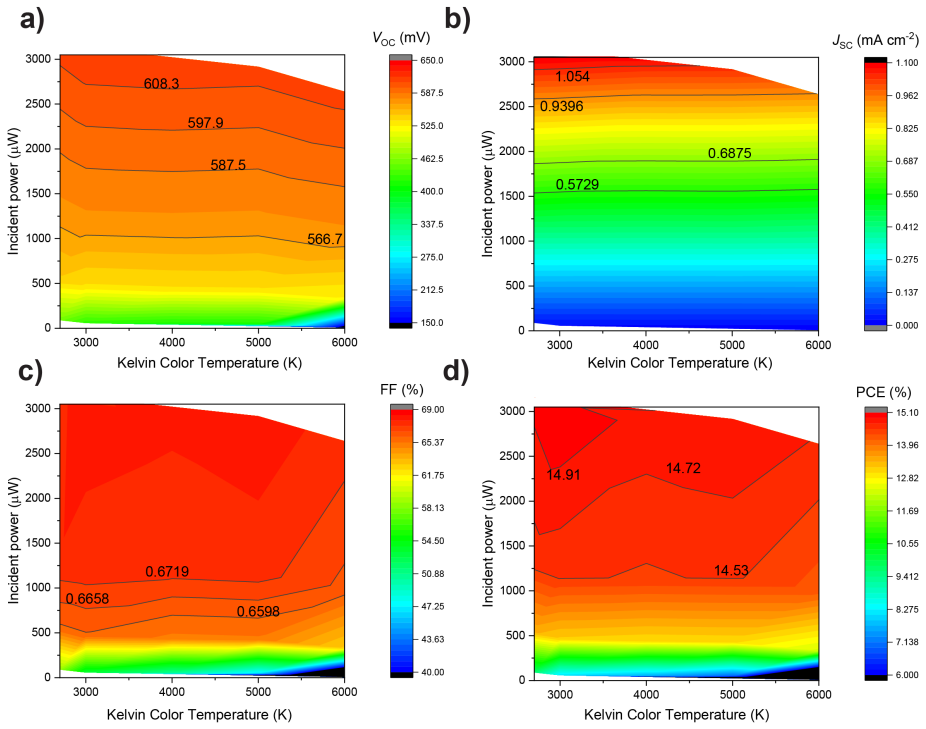

Figure 6. Filled contour plots of PV parameters for the CZTS device across a range of indoor lighting conditions, showing the effects of varying incident power and color temperature on (a)V_{OC}, (b) J_{SC}, (c) FF, and (d) PCE.

Figure 6 displays filled contour plots for V_{OC}, J_{SC}, FF, and PCE across the range of tested indoor lighting conditions. These plots illustrate the strong performance of CZTS solar cells under most conditions. As shown in **Figure 6a**, the device maintains a stable V_{OC} across various color temperatures and intensities, indicating effective charge separation and low recombination rates. The J_{SC} plot in **Figure 6b** reflects the device's capability to maintain decent current generation even as lighting conditions vary. In terms of FF (**Figure 6c**), the device consistently achieves values above 65% under moderate to high light intensities across all color temperatures, confirming the beneficial effects of high shunt resistance. This resilience against changes in lighting conditions makes CZTS solar cells particularly well-suited for indoor applications, where they may be exposed to a variety of artificial and natural light sources. Finally, the PCE plot (**Figure 6d**) reveals that the CZTS device achieves efficiencies exceeding 14.5% under most lighting conditions, with peak performance around 15.1% under 3000 K light at 100% intensity (2.93mW cm^{-2}). This level of efficiency is promising for indoor PV applications aimed at powering Internet of Things (IoT) devices.

This comprehensive testing illustrates the versatility of CZTS solar cells in adapting to various light sources typically found indoors, such as LEDs, fluorescent lamps, halogen lamps, and even indirect sunlight. Notably, the performance remains robust across all conditions, underscoring the potential of CZTS solar cells for indoor applications where light sources can vary significantly in intensity and spectral distribution, such as rooms that receive both artificial light and scattered sunlight.

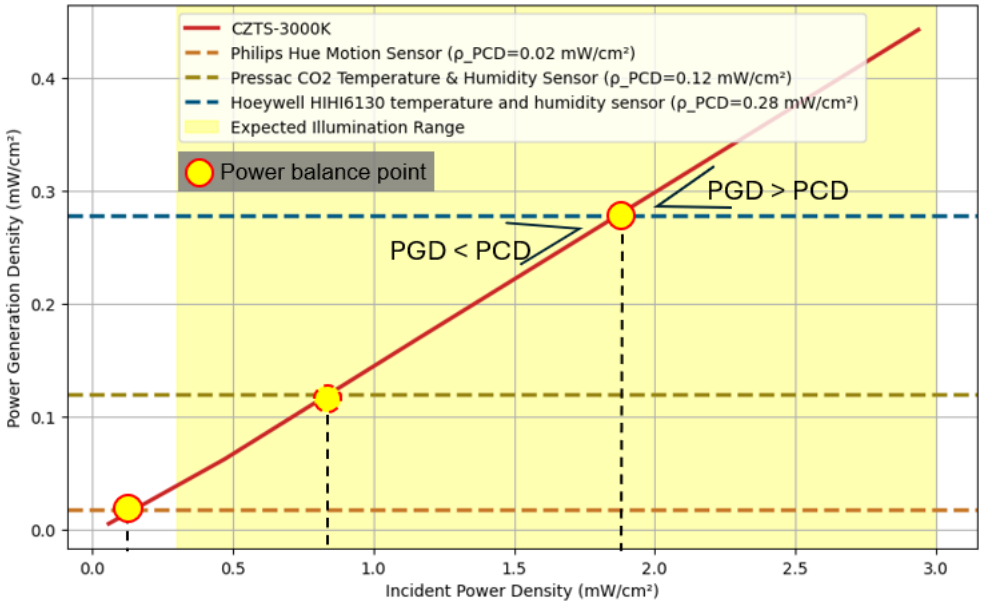

Figure 7. Simulation analysis of CZTS solar cells powering IoT devices under indoor lighting conditions (3000K). The graph shows the relationship between incident power density and power generation density (PGD) for the CZTS device under 3000K light. Horizontal lines represent the power consumption density (PCD) requirements for three IoT devices (0.02 mW/cm², 0.12 mW/cm², and 0.28 mW/cm²). The shaded yellow area indicates the typical indoor illumination range. When PGD exceeds PCD (right of the power balance point), the CZTS device generates sufficient power to operate the IoT device and store excess energy.

Building on the promising efficiency of CZTS solar cells under indoor lighting, we evaluated their practical application in powering commercial IoT devices—Device 1: Philips Hue Motion Sensor, Device 2: Pressac

CO2 Temperature & Humidity Sensor, and Device 3: Honeywell HIH6130 Temperature & Humidity Sensor—each with varying power demands of 0.02 mW cm^{-2}, 0.12 mW cm^{-2}, and 0.28 mW cm^{-2}, respectively, under indoor illumination. Detailed simulations regarding the powering of Devices 1–3 is summarized in the Supplementary Information. **Figure 7** illustrates the power generation density (PGD) of the CZTS solar cell under 3000 K lighting and its comparison with the power consumption density (PCD) of the IoT devices. The shaded yellow area represents the expected indoor light intensity range, between 0.3 and 3 mW cm^{-2}, which is typical for artificial lighting in indoor environments.

Table 1. Summary of the PV performance of the Ref and alkali-doped CZTS devices under various indoor illumination conditions.

Illumination	Incident power (mW cm^{-2})	V_{OC} (mV)	J_{SC} (mA cm^{-2})	FF (%)	PCE (%)
2700K-100%	3.157	616.2	1.14	67.7	14.97
2700K-50%	1.306	585.5	0.49	67.7	14.64
3000K-100%	2.938	619.2	1.06	68.1	15.06
3000K-50%	1.158	585.7	0.44	67.4	14.57
4000K-100%	2.884	618.1	1.03	67.9	14.83
4000K-50%	1.131	584.5	0.43	67.3	14.49
5000K-100%	2.916	621.2	1.04	68.2	14.87
5000K-50%	1.157	587.8	0.43	67.5	14.57
6000K-100%	2.638	617.2	0.94	67.5	14.70
6000K-50%	1.003	582.2	0.37	66.4	14.25
AM 1.5G	100.0	722.0	23.4	59.3	10.1

In this simulation, the PGD line intersects with the PCD requirements of each IoT device, revealing the minimum light intensities needed for each device to function. For IoT Device 1, which requires 0.02 mW cm^{-2} to operate, the PGD exceeds the PCD across the entire indoor light intensity range. This indicates that the CZTS solar cell can effectively power this device even under very low illumination conditions, with sufficient energy to meet the device's operational needs and potentially store excess energy. IoT devices with higher power demands, such as Device 2 (0.12 mW cm^{-2}) and Device 3 (0.28 mW cm^{-2}), require more intense illumination to reach the power balance point where PGD equals or surpasses PCD. For Device 2, this threshold is approximately 0.8 mW cm^{-2}, while for Device 3, it is around 1.85 mW cm^{-2}. Thus, Device 2 can operate in moderately low indoor lighting, whereas Device 3 requires more intense lighting—such as direct exposure to indoor LEDs—to function reliably.

These results demonstrate that the high efficiency of CZTS solar cells in indoor settings enables them to produce a sufficient amount of electrical energy, meeting the operational power requirements of various IoT devices. This adaptability to diverse indoor lighting conditions confirms CZTS solar cells as a promising technology for sustainable, self-powered IoT systems. Furthermore, the analysis provides a clear framework for determining the conditions under which CZTS solar cells can power specific devices, emphasizing their potential to drive low-power IoT networks in controlled environments like smart homes and offices.

Conclusion

This study demonstrates that Na–Li co-doping significantly enhances the performance of solution-processed Cu_2ZnSnS_4 (CZTS) solar cells. The co-doped devices achieved a power conversion efficiency (PCE) of 10.1% under standard AM 1.5G illumination and an impressive 15.1% under indoor lighting conditions (3000 K, 2.93 mW cm^{-2}), which is the highest reported efficiency for CZTS solar cells in indoor environments to date. The enhanced performance is attributed to the synergistic effects of Na and Li co-doping: Na promotes grain growth and reduces recombination at grain boundaries, improving charge

transport, while Li increases carrier concentration and passivates defects, leading to higher V_{OC} and FF. The co-doped CZTS solar cells exhibited exceptional adaptability under various indoor lighting conditions, maintaining high FF and stable V_{OC} across a range of color temperatures and light intensities. This adaptability underscores their suitability for indoor photovoltaic applications, particularly in powering low-power electronics like Internet of Things (IoT) devices.

These findings highlight Na–Li co-doping as an effective strategy to optimize CZTS solar cells for both outdoor and indoor applications. The approach leverages the individual benefits of each dopant to achieve significant improvements in device efficiency. Future research should focus on bandgap engineering to better align the absorber properties with indoor light spectra, potentially targeting an optimal bandgap range of 1.7 to 1.9 eV. These efforts could involve exploring alloying strategies within the kesterite family to further enhance device efficiency under indoor conditions. This work offers a promising pathway for advancing CZTS solar cells as efficient, non-toxic, and earth-abundant photovoltaic technologies suitable for sustainable energy solutions in indoor environments. The success of this co-doping strategy paves the way for the development of high-performance IPV kesterite devices, contributing to the growing demand for clean energy sources in powering next-generation electronics.

Conflicts of interest

There are no conflicts to declare.

Author contribution

Y. Gong: conceptualization, methodology, formal analysis, investigation, data curation, visualization, writing original draft; A. Jimenez-Arguijo: formal analysis, investigation, data curation, visualization; I. Caño-Prades: formal analysis, data curation; R.Scaffidi: formal analysis, investigation, data curation; C. Malerba: methodology, data curation; M. Valentini: methodology, data curation; D. Payno-Zarceño: methodology, data curation; A. Navarro-Güell: methodology; O. Segura-Blanch: methodology; D. Flandre: supervision; B. Vermang: supervision; A. Perez-Rodriguez: supervision; M. Placidi: supervision, funding acquisition; Z. Jehl Li-Kao: conceptualization, methodology, supervision; E. Saucedo: supervision, conceptualization, writing – review & editing, funding acquisition.

Acknowledgements:s

This project received funding from the European Union's H2020 research and innovation programme under grant agreement number 866018 (SENSATE), and by the Science Ministry of Spain projects number PID2023-148976OB-C41 (CURIO-CITY). The authors from UPC belong to the Micro and Nanotechnologies for Solar Energy Group (MNT-Solar) Consolidated Research Group of the "Generalitat de Catalunya" (2021 SGR 01286). Y.G. thanks the European Union's 616 Horizon 2020 research and innovation programme under the Marie Skłodowska-Curie grant agreement 618 No 10115148. R.S. thanks FWO for the funding through the Fundamental Research PhD Fellowship (1178024N) and Travel Grant for a long stay abroad (V462623N). D. P. and A.P. thanks projects SCALING (PID2022-138434OB-C52) and InnoPV (PID2022-140226OB-C31), funded by MCIN/AEI/10.13039/501100011033/ FEDER, UE. S.G. thanks the Serra Húnter programme. M.P. thanks InnoPV (PID2022-140226OB-C32) funded by MCIN/AEI/10.13039/501100011033/ FEDER, UE. Z. J. thanks financial support from Spanish Ministry of Science, Innovation through the Ramon y Cajal fellowship (RYC2021-033239-I). E.S. is grateful to ICREA Academia program.

Notes and references

[1] P. K. Nayak, S. Mahesh, H. J. Snaith, D. Cahen, Nat. Rev. Mater. 2019, 4, 269.
[2] I. Mathews, S. N. Kantareddy, T. Buonassisi, I. M. Peters, Joule 2019, 3, 1415.
[3] V. Pecunia, L. G. Occhipinti, R. L. Z. Hoye, Adv. Energy Mater. 2021, 11, 2100698.
[4] S. Giraldo, Z. Jehl, M. Placidi, V. Izquierdo-Roca, A. Pérez-Rodríguez, E. Saucedo, Adv. Mater. 2019, 31, 1806692.
[5] B. Li, B. Hou, G. A. J. Amaratunga, InfoMat 2021, 3, 445.
[6] D. Müller, E. Jiang, P. Rivas-Lazaro, C. Baretzky, G. Loukeris, S. Bogati, S. Paetel, S. J. C. Irvine, O. Oklobia, S. Jones, D. Lamb, A. Richter, G. Siefer, D. Lackner, H. Helmers, C. Teixeira, D. Forgács, M. Freitag, D. Bradford, Z. Shen, B. Zimmermann, U. Würfel, ACS Appl. Energy Mater. 2023, 6, 10404.
[7] X. Hou, Y. Wang, H. K. H. Lee, R. Datt, N. U. Miano, D. Yan, M. Li, F. Zhu, B. Hou, W. C. Tsoi, Z. Li, J. Mater. Chem. A 2020, 8, 21503.
[8] Y. Gong, Q. Zhu, B. Li, S. Wang, B. Duan, L. Lou, C. Xiang, E. Jedlicka, R. Giridharagopal, Y. Zhou, Q. Dai, W. Yan, S. Chen, Q. Meng, H. Xin, Nat. Energy 2022, 7, 966.
[9] Y. Gong, R. Qiu, C. Niu, J. Fu, E. Jedlicka, R. Giridharagopal, Q. Zhu, Y. Zhou, W. Yan, S. Yu, J. Jiang, S. Wu, D. S. Ginger, W. Huang, H. Xin, Adv. Funct. Mater. 2021, 31, 2101927.
[10] M. A. Green, E. D. Dunlop, M. Yoshita, N. Kopidakis, K. Bothe, G. Siefer, D. Hinken, M. Rauer, J. Hohl-Ebinger, X. Hao, Prog. Photovolt. Res. Appl. 2024, 32, 425.
[11] J. Park, H. Yoo, V. Karade, K. S. Gour, E. Choi, M. Kim, X. Hao, S. J. Shin, J. Kim, H. Shim, D. Kim, J. H. Kim, J. Yun, J. H. Kim, J. Mater. Chem. A 2020, 8, 14538.
[12] J. Park, M. Lee, V. Karade, S. J. Shin, H. Yoo, H. Shim, K. S. Gour, D. Kim, J. Hwang, D. Shin, J. Seidel, J. H. Kim, J. Yun, J. H. Kim, Sol. RRL 2021, 5, 2100020.
[13] V. C. Karade, J. Lim, K. S. Gour, J. S. Jang, S. J. Shin, J. H. Kim, B. S. Yang, H. Choi, T. Enkhbat, J. Kim, J. S. Yun, H. N. Jang, J. H. Yun, J. Park, J. H. Kim, J. Mater. Chem. A 2022, 10, 23831.
[14] J. K. W. Ho, H. Yin, S. K. So, J. Mater. Chem. A 2020, 8, 1717.
[15] M. Li, F. Igbari, Z. Wang, L. Liao, Adv. Energy Mater. 2020, 10, 2000641.
[16] M. C. Scharber, Sol. RRL 2024, 8, 2300811.
[17] A. Wang, J. Huang, C. Yan, G. He, X. Cui, X. Yuan, S. Zhou, M. He, T. Qiu, C. Zhao, M. A. Green, K. Sun, X. Hao, Adv. Funct. Mater. 2024, 2407063.
[18] M. Kumar, A. Dubey, N. Adhikari, S. Venkatesan, Q. Qiao, Energy Environ. Sci. 2015, 8, 3134.
[19] Y. E. Romanyuk, S. G. Haass, S. Giraldo, M. Placidi, D. Tiwari, D. J. Fermin, X. Hao, H. Xin, T. Schnabel, M. Kauk-Kuusik, P. Pistor, S. Lie, L. H. Wong, J. Phys. Energy 2019, 1, 044004.
[20] K. Yang, S. Kim, S. Kim, D. Son, J. Lee, Y. Kim, S. Sung, D. Kim, T. Enkhbat, J. Kim, J. Kim, W. Jo, J. Kang, Adv. Funct. Mater. 2021, 31, 2102238.
[21] Y. Gong, A. Jimenez-Arguijo, A. G. Medaille, S. Moser, A. Basak, R. Scaffidi, R. Carron, D. Flandre, B. Vermang, S. Giraldo, H. Xin, A. Perez-Rodriguez, E. Saucedo, Adv. Funct. Mater. 2024, 2404669.
[22] H. Liu, Y. Li, A. Xu, X. Li, C. Xiang, S. Zhou, S. Wang, W. Yan, H. Xin, Sol. RRL 2024, 2400588.
[23] Y. Liu, C. Hu, Y. Qi, W. Zhou, D. Kou, Z. Zhou, L. Han, Y. Meng, S. Yuan, S. Wu, Adv. Mater. Interfaces 2022, 9, 2201677.
[24] A. Jimenez-Arguijo, A. Navarro Güell, Y. Sanchez, C. Malerba, M. Valentini, P. Becker, L. Choubrac, T. Unold, Z. Jehl Li-Kao, S. Giraldo, E. Saucedo, Sol. RRL 2022, 6, 2200580.
[25] H. Xin, S. M. Vorpahl, A. D. Collord, I. L. Braly, A. R. Uhl, B. W. Krueger, D. S. Ginger, H. W. Hillhouse, Phys. Chem. Chem. Phys. 2015, 17, 23859.
[26] M. He, X. Zhang, J. Huang, J. Li, C. Yan, J. Kim, Y.-S. Chen, L. Yang, J. M. Cairney, Y. Zhang, S. Chen, J. Kim, M. A. Green, X. Hao, Adv. Energy Mater. 2021, 11, 2003783.
[27] Y. Gong, Y. Zhang, E. Jedlicka, R. Giridharagopal, J. A. Clark, W. Yan, C. Niu, R. Qiu, J. Jiang, S. Yu, S. Wu, H. W. Hillhouse, D. S. Ginger, W. Huang, H. Xin, Sci. China Mater. 2021, 64, 52.

[28] Y. Gong, Y. Zhang, Q. Zhu, Y. Zhou, R. Qiu, C. Niu, W. Yan, W. Huang, H. Xin, Energy Environ. Sci. 2021, 14, 2369.
[29] W. Chen, D. Dahliah, G.-M. Rignanese, G. Hautier, Energy Environ. Sci. 2021, 14, 3567.
[30] A. Crovetto, S. Kim, M. Fischer, N. Stenger, A. Walsh, I. Chorkendorff, P. C. K. Vesborg, Energy Environ. Sci. 2020, 13, 3489.
[31] X. Pan, X. Li, Y. Yang, C. Xiang, A. Xu, H. Liu, W. Yan, W. Huang, H. Xin, Adv. Energy Mater. 2023, 13, 2301780.
[32] S. Engberg, S. Canulescu, J. Schou, RSC Adv. 2018, 8, 7152.
[33] Y. Yang, L. Huang, D. Pan, ACS Appl. Mater. Interfaces 2017, 9, 23878.
[34] T. Maeda, A. Kawabata, T. Wada, Phys. Status Solidi C 2015, 12, 631.
[35] Z.-K. Yuan, S. Chen, Y. Xie, J.-S. Park, H. Xiang, X.-G. Gong, S.-H. Wei, Adv. Energy Mater. 2016, 6, 1601191.
[36] E. Jiang, C. Baretzky, D. Müller, O. Fischer, B. Zimmermann, U. Würfel, Sol. RRL 2024, 8, 2400303.